NANO LETTERS

Letter

pubs.acs.org/NanoLett

Ballistic Transport in Graphene Antidot Lattices

Andreas Sandner,[†] Tobias Preis,[†] Christian Schell,[†] Paula Giudici,[†] Kenji Watanabe,[‡] Takashi Taniguchi,[‡] Dieter Weiss,[†] and Jonathan Eroms*[,†]

[†]Institute of Experimental and Applied Physics, University of Regensburg, D-93040 Regensburg, Germany

[‡]National Institute for Materials Science, 1-1 Namiki, Tsukuba 305-0044, Japan

Supporting Information

ABSTRACT: The bulk carrier mobility in graphene was shown to be enhanced in graphene−boron nitride heterostructures. However, nanopatterning graphene can add extra damage and drastically degrade the intrinsic properties by edge disorder. Here we show that graphene embedded into a heterostructure with hexagonal boron nitride (hBN) on both sides is protected during a nanopatterning step. In this way, we can prepare graphene-based antidot lattices where the high mobility is preserved. We report magnetotransport experiments in those antidot lattices with lattice periods down to 50 nm. We observe pronounced commensurability features stemming from ballistic orbits around one or several antidots. Due to the short lattice period in our samples, we can also explore the boundary between the classical and the quantum transport regime, as the Fermi wavelength of the electrons approaches the smallest length scale of the artificial potential.

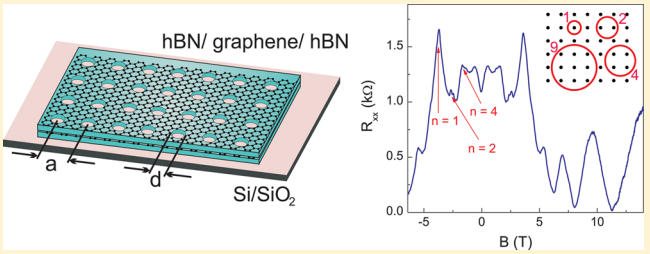

KEYWORDS: *Graphene, boron nitride, ballistic transport, nanopatterning, antidots*

Graphene samples can have a very high carrier mobility if influences from the substrate and the environment are minimized. Placing graphene on hexagonal boron nitride (hBN)[1,2] was shown to improve the carrier mobility,[3] allowing the observation of ballistic transport[4,5] or the fractional quantum Hall effect in bulk graphene.[6] Recently, a dry stacking technique was introduced, which allows complete encapsulation of graphene into layers of hBN and excludes any contamination from process chemicals such as electron beam resist.[7] Nanopatterning graphene can add extra damage and drastically reduce sample mobility by edge disorder.[8−10] Preparing etched graphene nanostructures on top of an hBN substrate instead of SiO_2 is no remedy, as transport characteristics are still dominated by edge roughness.[11] While chemically prepared graphene nanostructures[12−14] are a potential route for certain applications, the high flexibility of a top-down patterning approach is extremely desirable.

Here we show that etching fully encapsulated graphene on the nanoscale is more gentle and the high mobility can be preserved. To this end, we prepared antidot lattices[15] in graphene, where we observe magnetotransport features stemming from ballistic transport. We performed experiments on graphene antidot lattices[16,17] etched into hBN/graphene/hBN heterostructures with lattice periods going down to $a = 50$ nm. Due to the short lattice period in our samples, we can also explore the boundary between the classical and the quantum transport regime.

Antidot lattices show a beautiful realization of classical transport in mesoscopic systems. Furthermore, graphene antidot lattices can help circumventing the problem of the missing band gap in transistor applications[18,19] and were even predicted to serve as the technological basis for spin qubits.[20] In contrast to previous work on graphene on SiC,[17] we can determine and control the carrier density n_s on samples with different lattice periods. Thus, we can ensure unambiguously that magnetotransport on our samples shows commensurability features stemming from ballistic orbits around one or several antidots. This allows us to prove that the high carrier mobility is preserved in the nanopatterning step even though the zero field resistance is dominated by scattering on the artificial nanopattern, giving an apparent reduction of the mobility. The small feature size of our samples also allows us to approach the region where the classical picture of cyclotron orbits no longer applies. This classical to quantum crossover is governed by the ratio between the Fermi wavelength λ_F of the carriers and the dimensions of the nanopattern.

To obtain embedded graphene samples, hBN/graphene/hBN stacks were prepared using the dry stacking technique, patterned into Hall bar shape, and contacted using Cr/Au.[7] In hBN/graphene/hBN samples prepared by this method, we routinely obtained carrier mobilities in excess of $\mu = 100\,000$ $cm^2/(V\ s)$, showing all integer quantum Hall states starting from a few Tesla. In one sample without antidots and a mobility of $\mu = 300\,000$ $cm^2/(V\ s)$, we also observed the fractional quantum Hall effect at $T = 1.4$ K. This shows that our fabrication procedure is mature and consistently yields high

Received: October 30, 2015
Revised: November 18, 2015
Published: November 24, 2015

DOI: 10.1021/acs.nanolett.5b04414
Nano Lett. 2015, 15, 8402−8406

sample qualities. The samples presented in this study did not show any signs of a moiré superlattice.[21,22] Afterward, an antidot lattice was patterned. (For more details, see the Supporting Information.[23])

Figure 1 shows an optical micrograph of a finished sample and a scanning electron micrograph of a sample after measuring. A sketch of the antidot lattice, etched into the stack is also shown. The antidot lattice period a was varied between 50 and 250 nm. The antidot diameter d was lithographically defined to be about 40 nm, but due to the conical etching profile, the actual diameter in the graphene plane is smaller. Using SEM inspection, we estimate it to be about 25−30 nm.

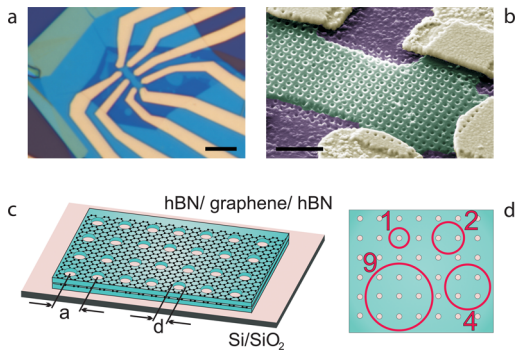

Figure 1. (a) Optical micrograph of a finished graphene Hall bar etched out of an hBN/graphene/hBN heterostructure and contacted with Cr/Au leads. Scale bar length 5 μm. (b) False-color scanning electron micrograph of a sample with lattice period a = 100 nm. Here, the heterostructure is shaded in green, the Cr/Au contacts yellow, and the Si/SiO_2 substrate violet. Scale bar length 500 nm. (c) Sketch of the antidot lattice in an hBN/graphene/hBN heterostructure. The antidot lattice period a ranges from 50 to 250 nm, and the antidot diameter d is about 25−30 nm. (d) The most prominent cyclotron orbits fitting into the lattice, giving rise to magnetoresistance peaks.

In Figure 2, we show data for a sample with a lattice period of a = 200 nm. From the gate response of the conductivity at a magnetic field B = 0, shown in Figure 2a, we calculate an apparent field effect mobility of μ = 35 000 $cm^2/(V\ s)$. At a carrier density n_S = 2.3× 10^{12} cm^{-2} this corresponds to an apparent mean free path of about $l_{mfp} = (\hbar/e)(\pi n_S)^{1/2}\mu$ = 620 nm. We estimate the intrinsic mean free path to be about 1400 nm.[23,24] Magnetotransport traces of this device (see Figure 2b) show pronounced peaks at field values where the cyclotron diameter $2R_C = (\hbar/eB)(\pi n_S)^{1/2}$ is commensurate to the square antidot lattice. The peak belonging to $2R_C = a$, the fundamental antidot peak, is most prominent. Additional peaks appearing at lower fields correspond to orbits encircling 2 and 4 antidots[15] (see Figure 1d), confirming a mean free path which spans several lattice periods. While in a simple picture only the unperturbed orbits encircling the antidots are responsible for the magnetotransport features, a more detailed analysis based on the Kubo formula shows that velocity correlations in the chaotic trajectories, which occupy the largest part of the phase space, result in the magnetoresistance peaks.[25,26] Most of the orbits therefore hit the antidot edges several times within a mean free path. Hence, the visibility of the antidot peaks not only proves a high bulk mobility but also shows that scattering at the edges does not cut off the trajectories, and we can conclude that the high carrier mobility also survives after nanopatterning.

At higher fields, the cyclotron diameter $2R_C$ is reduced below the neck width $a-d$ in between the antidots. We can observe Shubnikov−de Haas oscillations, eventually resulting in a well-defined quantum Hall effect. At B = 14 T we clearly observe the ν = 1 plateau, which again shows the high sample quality (Figure 2c). We evaluated the carrier density dependence of the magnetoresistance peaks corresponding to orbits around 1, 2, and 4 antidots (Figure 2d) and found that the peaks were always well-described by a square root dependence of the cyclotron diameter on the carrier density down to n_S = 3.2 × 10^{11} cm^{-2}. Quantitatively, we confirmed the formula for the cyclotron diameter for graphene given above, which contains spin and valley degeneracy.

Figure 3a shows the magnetoresistance of a sample with a = 100 nm at n_S = 2.8 × 10^{12} cm^{-2}. The apparent Hall mobility at this density is about μ = 8000 $cm^2/(V\ s)$. Again, scattering at the antidot potential limits the apparent mobility,[24] but the intrinsic mobility is higher as we clearly observe magnetoresistance peaks for n = 1, 2, 4 antidots, and a fourth peak at lower fields is weakly visible. Also, the ν = 1 quantum Hall state is visible in this sample, again indicating a higher intrinsic mobility.[23] Ishizaka and Ando studied how the visibility of the higher order antidot peaks depends on the mobility.[26] From their data, we estimate that the intrinsic mean free path must be at least 400 nm, well in excess of the apparent mean free path of 160 nm.[23]

The good visibility of the n = 2 peak confirms the small aspect ratio $d/a \leq 0.3$,[26] in agreement with our SEM analysis and also with the onset of the well-defined Shubnikov−de Haas oscillations in our magnetotransport data. All these approaches give an antidot diameter of d = 25−30 nm.

In experiments in GaAs based antidot lattices, it was found that, due to depletion at the antidot boundaries, the potential can be very soft and small lattice periods are hard to realize. In our case the data compares well to hard-wall potential lattices in GaAs, which could be realized in GaAs only at much larger lattice periods.[15] We also compared data for similar carrier densities in the electron and hole regime in Figure 3b and found the graphs to be virtually identical. This proves that there is no edge doping at the antidot boundaries, which would have led to different potential shapes in the electron and hole regime due to Fermi level pinning at the edges.

Now let us discuss the transition between the quantum and the classical transport regime. In GaAs-based heterostructures, the smallest lattice period realized so far was a = 80 nm and required critical tuning of the etch depth.[30] In contrast, due to the lack of a depletion region in graphene the fabrication of samples with a very small lattice period is less critical, and the carrier density is widely tunable. Also, due to valley degeneracy, the Fermi wavelength in graphene, $\lambda_F = 2(\pi/n_S)^{1/2}$ is a factor of $2^{1/2}$ larger than in GaAs based 2DEGs at the same carrier density. Thus, we can explore the transition from the semiclassical to the quantum regime,[31] where a description in terms of classical orbits is no longer justified. In the samples with $a \leq$ 100 nm we are able to study this transition. Figure 4a shows the disappearance of the main antidot peak in a sample with a = 75 nm as the carrier density is lowered, making λ_F longer. We find that this peak is only visible at densities above n_S = 4.3 × 10^{11} cm^{-2}, corresponding to λ_F = 54 nm. Also, in two samples with a = 100 nm, we observe that the main antidot peak becomes visible for densities larger than n_S = 2.2 × 10^{11} cm^{-2}, which corresponds to λ_F = 75 nm. In a sample with a = 50 nm, we observed a weak antidot peak only at n_S = 2.5× 10^{12}

DOI: 10.1021/acs.nanolett.5b04414
Nano Lett. 2015, 15, 8402−8406

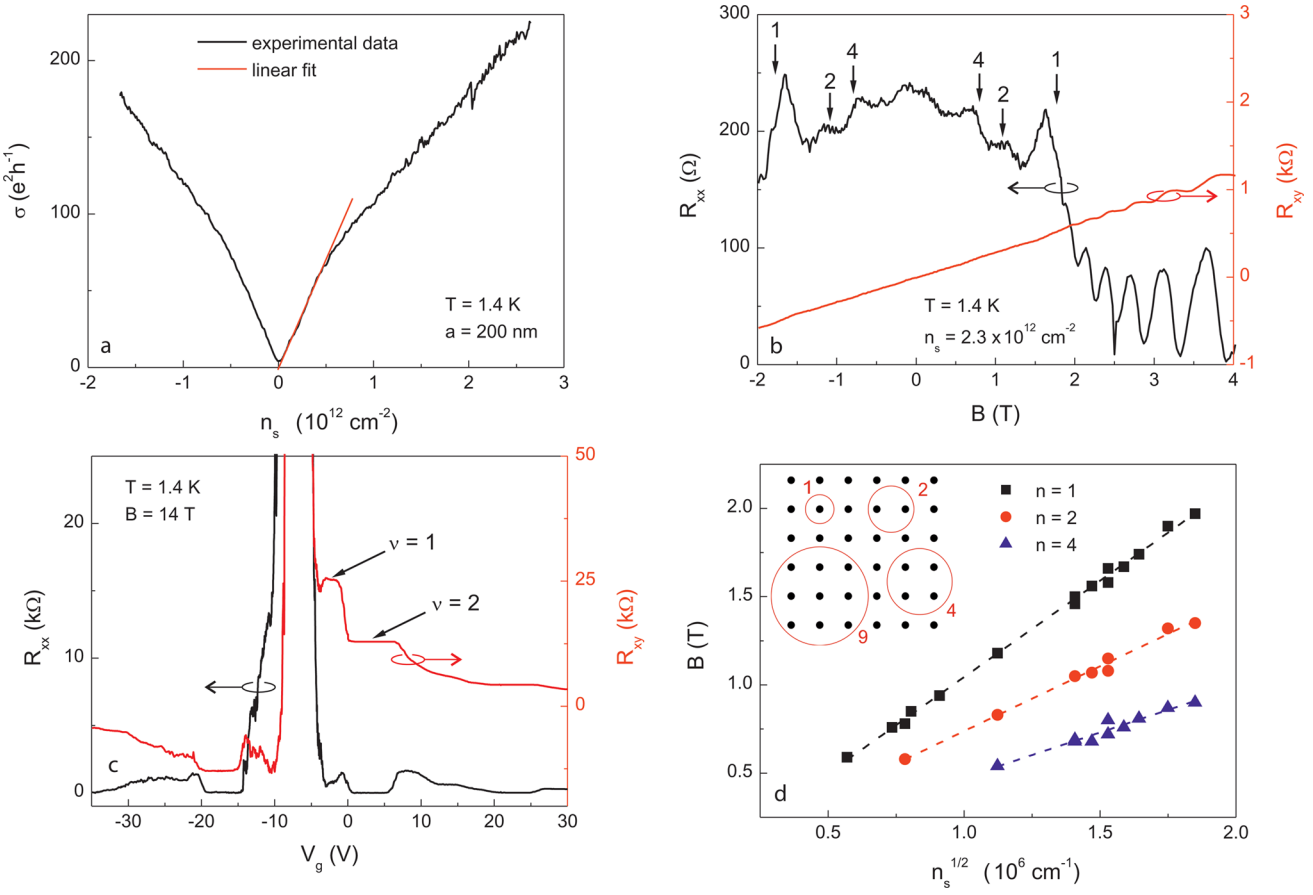

Figure 2. (a) Gate dependence of the sheet conductivity of a sample with a = 200 nm. The linear fit gives an apparent mobility of μ = 35 000 cm^2/(V s). (b) Magnetoresistance and Hall resistance. The arrows correspond to the expected magnetic field positions of the orbits sketched in Figure 1d. The fine structure in R_{xx} is not noise, but phase-coherent oscillations[27−29] that disappear at higher temperatures. (c) Gate dependence of R_{xx} and R_{xy} at B = 14 T, showing a clear ν = 1 quantum Hall plateau. This feature is only observed in high-mobility graphene devices. (d) The magnetic field positions of the three antidot peaks scale with the square root of the carrier density, confirming the classical nature of those peaks.

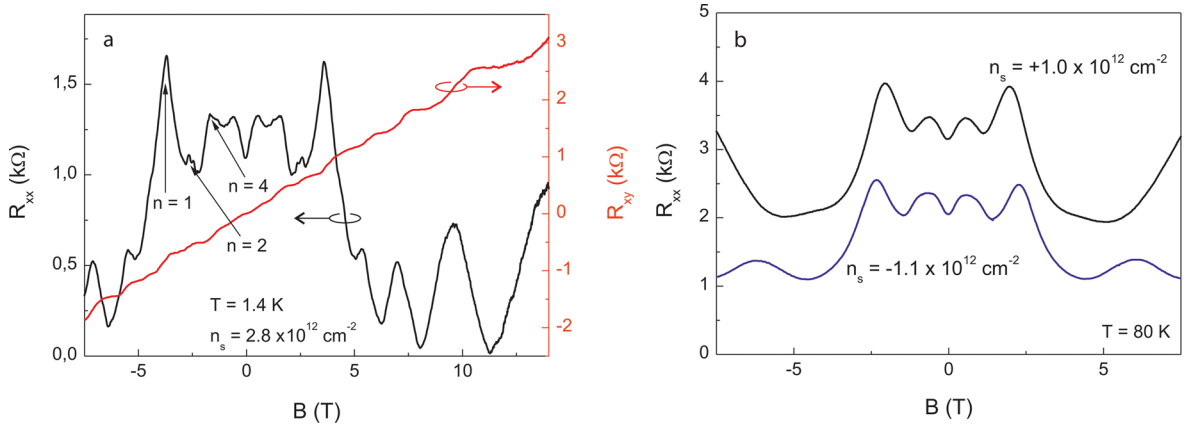

Figure 3. (a) Magnetoresistance and Hall resistance data taken on a sample with a = 100 nm. The three well-defined antidot peaks correspond to orbits around 1, 2, and 4 antidots. (b) R_{xx} taken at similar electron and hole density. Here, T = 80 K to show the classical features more clearly. There is virtually no difference between those graphs, proving that the potential profile is the same for electrons and holes.

cm^{-2}(λ_F = 22 nm). To be in the classical limit of a quantum system, the Fermi wavelength must satisfy a condition $\lambda_F/2\pi \ll l$,[32] where l is a typical dimension of the system. In our case, the neck width $a-d$ of the constriction between the antidots is the shortest length scale in the problem, and we find that when $\lambda_F \approx a-d$ the classical regime sets in and the antidot peak becomes visible.

The fact that the antidot peaks disappear at low densities cannot be attributed to a relative increase of disorder such as deviation of the position and diameter of the antidots in our system, since we see well-defined features without any deviation at higher densities. The suppression of the commensurability peaks can be either due to a limited mean free path or the breakdown of the classical picture. In Figure 2d (lattice period a

DOI: 10.1021/acs.nanolett.5b04414
Nano Lett. 2015, 15, 8402−8406

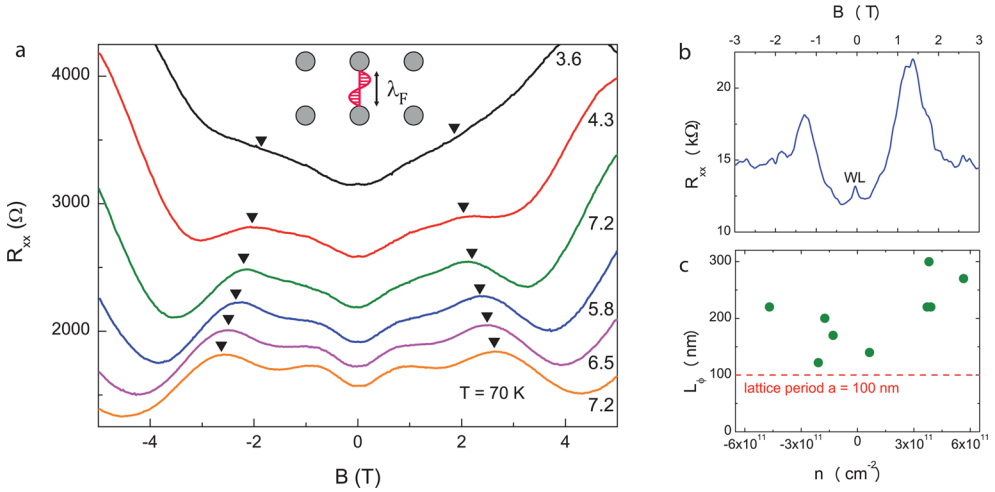

Figure 4. (a) R_{xx} data of a sample with a = 75 nm taken at very low densities, at the transition into the regime of classical transport. The densities n_S are given in units of 10^{11} cm^{-2}, shown next to the corresponding graphs. The expected position of the main antidot peak is marked with a triangle for each density. A higher order antidot peak is also visible at lower magnetic fields. As the carrier density is lowered, the antidot peaks disappear. Inset: Sketch of the Fermi wavelength corresponding to the $n_S = 4.3 \times 10^{11}$ cm^{-2}. (b) Weak localization (WL) peak in the sample with a = 100 nm, taken at $n_S = 1.3 \times 10^{11}$ cm^{-2}. The antidot peak is not visible at this low density, the big peaks at $B = \pm 1.4$ T are a Shubnikov–de Haas oscillation. (c) Phase coherence length taken from the weak localization fits of a sample with a = 100 nm at various low densities and T = 1.4 K. The phase coherence length exceeds the lattice period, showing that the etched boundaries do not lead to severe phase-breaking.

= 200 nm), all the antidot peaks disappear at roughly the same magnetic field, $B \approx 0.5$ T (where μB exceeds some constant), but different carrier density. This behavior is clearly governed by a limited mean free path. In contrast, in the sample of Figure 4a (a = 100 nm), we find that the classical features at both $B \approx 1$ T and $B \approx 2.5$ T disappear at the same carrier densities, making a λ_F-driven scenario more realistic.

Finally, at low densities, we can observe a weak localization (WL) feature at low temperatures: a peak in the magnetoresistance at $B = 0$ (see Figure 4b). Using a standard analysis for WL in graphene[33] that we employed in earlier work on graphene antidot lattices on SiO_2,[16] we extracted the phase coherence length L_ϕ. For the sample with a = 100 nm (same as in Figure 3a), we found it to be between 120 and 300 nm (see Figure 4c). It clearly exceeds the lattice period, unlike in graphene antidot samples on SiO_2 where L_ϕ was significantly below a.[16] We therefore again conclude that nanopatterning of embedded graphene leads to greatly reduced scattering at the sample edges.

In summary, we prepared antidot lattices in stacks of hBN/graphene/hBN and observed well-developed commensurability features in samples with lattice periods from a = 50 nm to a = 250 nm. This shows that the etching procedure preserves the high sample quality. In the short-period graphene samples, we could observe the disappearance of classical features when the Fermi wavelength λ_F exceeds $a-d$, marking a classical to quantum transition. Our experiments therefore pave the way for well-controlled graphene based nanodevices. For example, in triangular antidot lattices[34] in graphene, Hofstadter butterflies and magnetic band gap closing were predicted,[35] which are now experimentally within reach.

■ ASSOCIATED CONTENT

Supporting Information

The Supporting Information is available free of charge on the ACS Publications website at DOI: 10.1021/acs.nanolett.5b04414.

Fabrication details, determination of the intrinsic mean free path, antidot diameter, additional data, and the validity of the classical picture (PDF)

■ AUTHOR INFORMATION

Corresponding Author

*E-mail: jonathan.eroms@ur.de. Fax: +49 941 943-3196.

Present Address

P.G.: Consejo Nacional de Investigaciones Científicas y Técnicas (CONICET), Buenos Aires, Argentina.

Notes

The authors declare no competing financial interest.

■ ACKNOWLEDGMENTS

The authors thank A. Geim and R. Jalil for sharing details of the graphene transfer procedure, R. Fleischmann, T. Geisel and K. Richter for helpful discussions, and the Deutsche Forschungsgemeinschaft (DFG) for funding through projects GRK 1570 and GI 539/4-1.

■ REFERENCES

(1) Kubota, Y.; Watanabe, K.; Tsuda, O.; Taniguchi, T. *Science* **2007**, *317*, 932–934.

(2) Taniguchi, T.; Watanabe, K. *J. Cryst. Growth* **2007**, *303*, 525–529.

(3) Dean, C. R.; Young, A. F.; Meric, I.; Lee, C.; Wang, L.; Sorgenfrei, S.; Watanabe, K.; Taniguchi, T.; Kim, P.; Shepard, K. L.; Hone, J. *Nat. Nanotechnol.* **2010**, *5*, 722–726.

(4) Taychatanapat, T.; Watanabe, K.; Taniguchi, T.; Jarillo-Herrero, P. *Nat. Phys.* **2013**, *9*, 225–229.

(5) Calado, V. E.; Zhu, S.-E.; Goswami, S.; Xu, Q.; Watanabe, K.; Taniguchi, T.; Janssen, G. C. A. M.; Vandersypen, L. M. K. *Appl. Phys. Lett.* **2014**, *104*, 023103.

(6) Dean, C. R.; Young, A. F.; Cadden-Zimansky, P.; Wang, L.; Ren, H.; Watanabe, K.; Taniguchi, T.; Kim, P.; Hone, J.; Shepard, K. L. *Nat. Phys.* **2011**, *7*, 693–696.

(7) Wang, L.; Meric, I.; Huang, P. Y.; Gao, Q.; Gao, Y.; Tran, H.; Taniguchi, T.; Watanabe, K.; Campos, L. M.; Muller, D. A.; Guo, J.; Kim, P.; Hone, J.; Shepard, K. L.; Dean, C. R. *Science* **2013**, *342*, 614–617.

DOI: 10.1021/acs.nanolett.5b04414
Nano Lett. 2015, 15, 8402–8406

(8) Stampfer, C.; Güttinger, J.; Hellmüller, S.; Molitor, F.; Ensslin, K.; Ihn, T. *Phys. Rev. Lett.* **2009**, *102*, 056403.
(9) Poumirol, J.-M.; Cresti, A.; Roche, S.; Escoffier, W.; Goiran, M.; Wang, X.; Li, X.; Dai, H.; Raquet, B. *Phys. Rev. B: Condens. Matter Mater. Phys.* **2010**, *82*, 041413.
(10) Minke, S.; Jhang, S. H.; Wurm, J.; Skourski, Y.; Wosnitza, J.; Strunk, C.; Weiss, D.; Richter, K.; Eroms, J. *Phys. Rev. B: Condens. Matter Mater. Phys.* **2012**, *85*, 195432.
(11) Bischoff, D.; Krähenmann, T.; Dröscher, S.; Gruner, M. A.; Barraud, C.; Ihn, T.; Ensslin, K. *Appl. Phys. Lett.* **2012**, *101*, 203103.
(12) Jiao, L.; Zhang, L.; Wang, X.; Diankov, G.; Dai, H. *Nature* **2009**, *458*, 877−880.
(13) Kosynkin, D. V.; Higginbotham, A. L.; Sinitskii, A.; Lomeda, J. R.; Dimiev, A.; Price, B. K.; Tour, J. M. *Nature* **2009**, *458*, 872−876.
(14) Cai, J.; Ruffieux, P.; Jaafar, R.; Bieri, M.; Braun, T.; Blankenburg, S.; Muoth, M.; Seitsonen, A. P.; Saleh, M.; Feng, X.; Mullen, K.; Fasel, R. *Nature* **2010**, *466*, 470−473.
(15) Weiss, D.; Roukes, M. L.; Menschig, A.; Grambow, P.; von Klitzing, K.; Weimann, G. *Phys. Rev. Lett.* **1991**, *66*, 2790−2793.
(16) Eroms, J.; Weiss, D. *New J. Phys.* **2009**, *11*, 095021.
(17) Shen, T.; Wu, Y. Q.; Capano, M. A.; Rokhinson, L. P.; Engel, L. W.; Ye, P. D. *Appl. Phys. Lett.* **2008**, *93*, 122102.
(18) Bai, J.; Zhong, X.; Jiang, S.; Huang, Y.; Duan, X. *Nat. Nanotechnol.* **2010**, *5*, 190−194.
(19) Kim, M.; Safron, N. S.; Han, E.; Arnold, M. S.; Gopalan, P. *Nano Lett.* **2010**, *10*, 1125−1131.
(20) Pedersen, T. G.; Flindt, C.; Pedersen, J.; Mortensen, N. A.; Jauho, A.-P.; Pedersen, K. *Phys. Rev. Lett.* **2008**, *100*, 136804.
(21) Dean, C. R.; Wang, L.; Maher, P.; Forsythe, C.; Ghahari, F.; Gao, Y.; Katoch, J.; Ishigami, M.; Moon, P.; Koshino, M.; Taniguchi, T.; Watanabe, K.; Shepard, K. L.; Hone, J.; Kim, P. *Nature* **2013**, *497*, 598−602.
(22) Ponomarenko, L. A.; et al. *Nature* **2013**, *497*, 594−597.
(23) See Supporting Information for fabrication details, determination of the intrinsic mean free path, antidot diameter, additional data, and the validity of the classical picture.
(24) Ishizaka, S.; Ando, T. *Phys. Low-Dim. Struct.* **1999**, *5-6*, 5−12.
(25) Fleischmann, R.; Geisel, T.; Ketzmerick, R. *Phys. Rev. Lett.* **1992**, *68*, 1367−1370.
(26) Ishizaka, S.; Ando, T. *Phys. Rev. B: Condens. Matter Mater. Phys.* **1997**, *55*, 16331−16338.
(27) Nihey, F.; Nakamura, K. *Phys. B* **1993**, *184*, 398−402.
(28) Weiss, D.; Richter, K.; Menschig, A.; Bergmann, R.; Schweizer, H.; von Klitzing, K.; Weimann, G. *Phys. Rev. Lett.* **1993**, *70*, 4118−4121.
(29) Schuster, R.; Ensslin, K.; Wharam, D.; Kühn, S.; Kotthaus, J. P.; Böhm, G.; Klein, W.; Tränkle, G.; Weimann, G. *Phys. Rev. B: Condens. Matter Mater. Phys.* **1994**, *49*, 8510−8513.
(30) Kozlov, D.; Kvon, Z.; Plotnikov, A.; Latyshev, A. *JETP Lett.* **2010**, *91*, 134−138.
(31) Brack, M.; Bhaduri, R. K. In *Semiclassical Physics*; Pines, D., Ed.; Addison-Wesley, 1997.
(32) Sakurai, J. J. In *Modern Quantum Mechanics*; Tuan, S. F., Ed.; Addison-Wesley, 1994.
(33) McCann, E.; Kechedzhi, K.; Fal'ko, V. I.; Suzuura, H.; Ando, T.; Altshuler, B. L. *Phys. Rev. Lett.* **2006**, *97*, 146805.
(34) Takahara, J.; Nomura, A.; Gamo, K.; Takaoka, S.; Murase, K.; Ahmed, H. *Jpn. J. Appl. Phys.* **1995**, *34*, 4325.
(35) Pedersen, J. G.; Pedersen, T. G. *Phys. Rev. B: Condens. Matter Mater. Phys.* **2013**, *87*, 235404.
(36) Yagi, R.; Sakakibara, R.; Ebisuoka, R.; Onishi, J.; Watanabe, K.; Taniguchi, T.; Iye, Y. *Phys. Rev. B: Condens. Matter Mater. Phys.* **2015**, *92*, 195406.

■ NOTE ADDED IN PROOF

After submission of our manuscript we became aware of related work by Yagi et al.[36]

DOI: 10.1021/acs.nanolett.5b04414
Nano Lett. 2015, 15, 8402−8406